



Numerical simulation of liquid emptying of micro-cavities as a model of gravure printing applications

Diego M. Campana

Instituto de Desarrollo Tecnológico para la Industria Química (INTEC-CONICET), Güemes 3450, Santa Fe (3000),
Argentina
dcampana@santafe-conicet.gov.ar

Marcio S. Carvalho

Department of Mechanical Engineering, Pontifícia Universidade Católica do Rio de Janeiro (PUC-RIO), Rio de Janeiro, RJ 22453-900,
Brazil
msc@puc-rio.br

Abstract. *In the last years, printing techniques have gained much attention because its applicability in the production of electronics devices, like polymer solar cells, flat panel displays (LCD) and other general purposes electronics circuits. Roto-gravure printing is a specially attractive roll-to-roll procedure, because its high accuracy and production rate. The term gravure comes from the fact that one of the rolls has a pattern engraved in its surface, which is made of tinny cells or cavities containing fluid that is transferred by direct contact to the final substrate. In this work it is solved the stretching of a 2D planar liquid filament between a fixed cavity and a moving plane plate, to model the liquid transfer in a gravure printing unit. To mimic the kinematic of the real process, the plate is moved with a velocity obtained from a complete kinematics analysis of a roll to roll system. The fluid flow problem is modeled by solving the Navier-Stokes equations, which are discretized with the finite element method; the free surfaces evolution and resulting domain deformation are tracked by a pseudo-solid mesh deforming algorithm. The results predict that as the roll radius is reduced, thus increasing the lateral and rotation velocities of the top plate relative to the cavity, more liquid is removed from it. However, due to an increase in the lateral displacement of the liquid bridge, special care must be taken in the wettability properties of the substrate to avoid severe errors in the pattern fidelity. When the roll radius and cavity geometry are fixed, the simulations predict a strong non-linear behavior of the liquid fraction extracted from the cavity versus capillary number. The results shown that to obtain a good description of the process in a wide range of operating conditions, it is important to introduce an appropriate kinematic for the moving surface.*

Keywords: *Liquid bridges, free surfaces, gravure printing, finite elements*

1. INTRODUCTION

In the last years, printing techniques have gained much attention because its potential applicability in the production of flexible electronics devices. One important example is the production of polymer solar cells, which are a promising solution in the reduction of the high cost photovoltaic technologies (Krebs, 2009). Polymer solar cells are suitable to be manufactured by using high scale film-forming techniques like slot and gravure coating and also by printing technologies like screen, pad or gravure printing (Santa-Nokki *et al.*, 2006; Ding *et al.*, 2009). The high production rate and low manufacturing cost are crucial factors to compensate the low efficiency conversion these devices have at present (Krebs, 2009). Another common example of electronic device that can be manufactured by printing techniques is flat panel displays which are formed by thousands of light emitting diodes or LEDs (Lee *et al.*, 2010b; Chung *et al.*, 2010). Also, gravure and offset printing techniques have been successfully tested to print general purpose small scale electronic circuits on flexible substrates (Lee *et al.*, 2010a; Pudas *et al.*, 2004b,a).

Among the many used printing techniques, gravure is very attractive because it allows printing tiny patterns (in the order of 10 microns) using liquids of medium viscosities (up to 1000 cP) and at fast substrate velocity (10 m/s and higher), when a roll-to-roll configuration is used (Krebs, 2009). The term gravure comes from the fact that one of the rolls has a pattern engraved on its surface, which is made of small cells or cavities. They are filled with the liquid as the surface of the rolls rotate inside a bath, then a blade removes the excess of liquid and finally the cavities are emptied by direct contact, thereby transferring the engraved pattern to a second surface (usually, the final substrate).

To model the liquid transfer from a cavity to a surface, the usual simplification has been to consider the stretching of a planar or axisymmetric liquid filament between a moving surface (flat plate) and a fixed trapezoidal cavity. The main goals are usually to determine the mass fraction of liquid that is transferred from the cavity to the moving surface (usually denoted as ϕ and also called pickup fraction) as a function of contact angles, surface velocity, geometry of the cavity and flow parameters. Hoda and Kumar (2008) used the boundary integral method to study the removal of liquid from 2D planar grooves with rectangular cross sections. By imposing simultaneously shear (horizontal) and stretching (vertical) velocities to the upper plate, the authors predicted the residual liquid fraction left in the cavity for different cavity aspect ratios and stretching velocities, while the capillary number Ca was kept fixed ($Ca = 0.01$). Their results show that almost all the liquid inside the cavity can be removed when the stretching velocity is higher than a critical value, which is

a function of the cavity aspect ratio. The predictions indicated that wider cavities are easier to empty. Finally, they also made few simulations introducing a combination of shear and rotational motion to the upper plate, finding that rotation tends to increase the liquid fraction removed from the cavity.

Up to our knowledge, the most recent work on liquid transfer from a cavity to a surface motivated by printing applications is that presented by Dodds *et al.* (2009). The main objective was to explore the behavior of axisymmetric liquid bridges being stretched between a plate and cavities with trapezoidal cross sections. They used the Galerkin finite element method to solve the Navier-Stokes equations and an elliptic mesh generation equation was used to map the physical and computational domains (Christodoulou *et al.*, 1997). Their results show that the volume fraction ϕ rises as the cavity is made wider and that ϕ increases with the capillary number.

Because the inherent complexity in the observation and measurements of such small-scale interfacial fluid flow, few experimental analysis are available. Good examples are those presented by Yin and Kumar (2006) and Chuang *et al.* (2008). Actually, to simplify both the visualization process and the measurements of transferred liquid fractions, they used up-scaled engraved cavities with characteristic dimensions in the order of millimeters, much larger than actual cavities used in gravure printing. More specifically, Yin and Kumar (2006) made experiments to visualize the process of emptying of a single cell (width \times length = 1.5 \times 1 mm). By filling the cavities at different levels, they emptied the cell by displacing horizontally a top curved surface at different velocities. The setup allowed visualization of the flow field during the process and they could observe different flow patterns, mainly depending on both the initial level of the liquid in cavity and the gap between the cavity and the moving surface. They found that the extracted liquid fraction reaches maximum values close to $\phi = 0.5$ for low capillary numbers ($Ca \sim 10^{-4}$) and then decrease monotonically up to $Ca \sim 5 \times 10^{-2}$. Chuang *et al.* (2008) used trapezoidal cavities similar to those of Yin and Kumar (2006). They also made arrays of up to 4 cavities to study how their interaction affects the transferred volume fraction ϕ . To simulate the gravure printing process, they passed a roller at different velocities and gaps. The range of the capillary number explored was small ($2.5 \times 10^{-3} < Ca < 3 \times 10^{-2}$), but they also observed a decrease in ϕ as Ca rises.

Summarizing, the available experimental results suggest that the transferred liquid fraction decreases as capillary number rises, at least in the explored range. By contrast, Dodds *et al.* (2009) presented results for two values of capillary numbers ($Ca = 0.1$ and 0.01) and their predictions suggest that the liquid fraction ϕ decrease as capillary number falls; thus, new results are needed to close the gap between simulations and experiments.

In the present work, we also solve numerically the free surface flow that occurs during the process of liquid transfer from a fixed 2D planar trapezoidal cavity and a moving plate, as an effort to understand the fundamental aspects involved in gravure printing operations. As was shown by the works of Hoda and Kumar (2008) and Dodds *et al.* (2012), the relative motion of rotation and shear affects the liquid transfer. Thus, we develop an expression for the relative velocity of the plate based on a kinematic model of a roll-to-roll system (Section 2.1). This allows to us to consider stretching (vertical), shearing (horizontal) and rotational velocities in a coherent manner and related to the operational parameter of the process. To model the fluid flow we solved the Navier-Stokes equations with appropriate boundary conditions, which are detailed in Section 2.2 and implemented a robust numerical algorithm to solve them, which is discussed in Section 3.

We discuss the effects of the moving surface kinematics and cavity aspect ratio on the transferred liquid fraction ϕ in Section 4.2, while examine the influence of capillary number and other important aspects of printing applications in Section 4.3. Finally, in Section 5 we present the main conclusions of this work and some future research directions.

2. THE MODEL

2.1 Kinematic description of a rotational gravure printing system

Figure 1 shows the schematic configuration of two equal counter rotating rolls separated by a gap H_0 . The positions of points on both roll surfaces are defined by the angles θ_1 and θ_2 with respect to the horizontal line, as shown in the figure. The angles $\theta_1 = \theta_2 = \omega t + \theta_0 = \theta$, while θ_0 is introduced to include the possibility to consider an initial inclination or twist of the plate with respect to the cavity. However, this issue will not be explored in this work and for all situations analyzed here $\theta_0 = \pi/2$: points C and O are initially located in the minimum gap plane. The bottom roll represents the engraved roll having the cavities and only one cavity is sketched (dark gray color) to simplify the diagram. Figure 1 shows two frames of reference. One frame (F_1) is fixed at the center of the bottom roll and is defined by the unit vectors $(\mathbf{i}', \mathbf{j}', \mathbf{k}')$. The coordinates of any point with respect to this frame are represented by (x', y', z') . The second frame of reference (F_2) is attached to the center of the cell surface (point O) and therefore is moving with respect to the fixed frame F_1 . The coordinates of any point with respect to the moving frame F_2 are represented by (x, y, z) . The goal is to derive an expression for the velocity \mathbf{V}_w of points on the vicinity of C , respect to the moving frame F_2 . Because the area wetted by the liquid will be usually very small respect to the roll radius, we can safely represents those points as belonging on small plane rotating with angular velocity $\omega_r = \omega$ around the point C .

After some basic kinematic transformations, not detailed here for brevity, we can demonstrate that the final expression

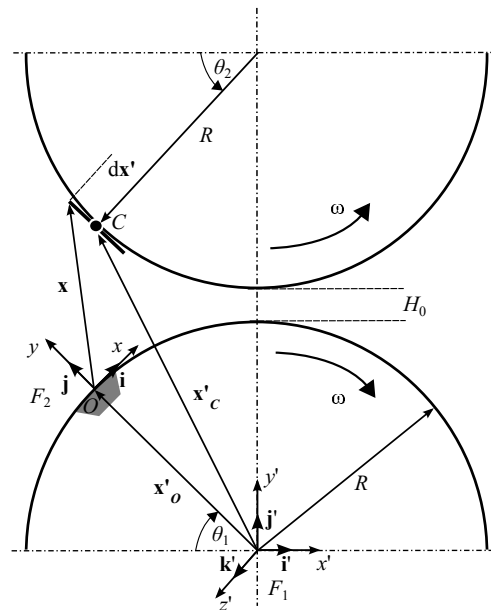


Figure 1. Geometric model, variables and frames used to describe the relative motion between the cavity and points on the top roll surface.

for the velocity of points on this top plane respect to frame F_2 , is

$$\begin{aligned} \mathbf{V}_w(\mathbf{x}, t) &= [-2\omega R \cos^2(\theta) - 2\omega_r y + \omega_r y_C] \mathbf{i} + [-2\omega R \cos(\theta) \sin(\theta) + 2\omega_r x - \omega_r x_C] \mathbf{j}, \\ x_C &= |\mathbf{x}'_C - \mathbf{x}'_O| \cos(\theta), y_C = |\mathbf{x}'_C - \mathbf{x}'_O| \sin(\theta), \\ |\mathbf{x}'_C - \mathbf{x}'_O| &= 2R + H_0 - 2R \sin(\theta). \end{aligned} \quad (1)$$

As mentioned before, all cases discussed here consider that the initial condition is such that the cavity and substrate are in horizontal position ($\theta = \pi/2$). From this initial condition, the top roll surface evolves according to Eq. 1, while the cavity remains fixed. It is clear that the resulting kinematics given by Eq. 1 is a combination of shear (horizontal), extension (vertical) and rotational velocities of the plate. Another important issue to be considered here is the selection of the velocity scale for the problem. Because the cavity and plate surfaces have the same tangential velocity, $V_t = \omega R$ does not represent a correct scale at all for the filament stretching, but a more appropriate velocity scale is the stretching vertical velocity at which those surfaces separate. It is very easy to show that this vertical velocity scale is given by $V_E = V_t \sqrt{2(L_b/R - (L_b/R)^2)}$ (Dodds, 2011). In the above expression, L_b represents a breakup length, i.e. the vertical distance between the plate and cavity at which the liquid filament breaks. Simulations performed in both Dodds *et al.* (2009) and in this work show that $L_b \sim 5\delta$, being δ the depth of the cavity, which will be used as the length scale. Typical values of the above magnitudes in gravure printing systems are $V_t = 10$ m/s, $\delta = 10 \mu\text{m}$ and $R = 10$ in = 0.254 m. Thus, $V_E \sim V_t \sqrt{10\delta/R} \sim 0.2$ m, that is, two orders of magnitude smaller than V_t . Thus, by selecting V_E , δ and δ/V_E as scales of velocity, length and time, respectively, the dimensionless expression for the plate velocity is

$$\mathbf{V}_w(\mathbf{x}, t) = [-2\omega_b R_b \cos^2(\theta) - 2\omega_p y + \omega_p y_C] \mathbf{i} + [-2\omega_b R_b \cos(\theta) \sin(\theta) + 2\omega_p x - \omega_p x_C] \mathbf{j}, \quad (2)$$

In Equation 2, \mathbf{V}_w , x , y , x_C , y_C and $\theta = \omega_b t + \theta_0$ are now redefined dimensionless quantities, while $V_E = V_t \sqrt{10/R_b}$, $\omega_b = \omega \delta / V_E$, $\omega_p = \omega_r \delta / V_E$ and $R_b = R / \delta$.

In cases when $R_b \gg 1$ and because $\theta \sim \pi/2$, which implies that $\cos^2(\theta) \ll \cos(\theta) \sin(\theta)$, Eq. (2) can be simplified to

$$\mathbf{V}_w(\mathbf{x}, t) = -2\omega_b R_b \cos(\theta) \mathbf{j}. \quad (3)$$

In summary, for cases when the roll size R is much bigger than cavity size δ , the kinematic of the system can be approached as a pure extensional motion given by Eq. 3. Note that this limiting case can be recovered from Eq. 2 by simply doing $\omega_p = 0$; this characteristic will be used in the results to compare the pure extensional case from the general cases including extension, shearing and rotation.

2.2 Flow equations and boundary conditions

The differential equations and the appropriate boundary conditions that describe this transient, free surface flow with contact lines are presented in this section. The flow domain and the relevant geometric parameters are shown in Fig. 2.

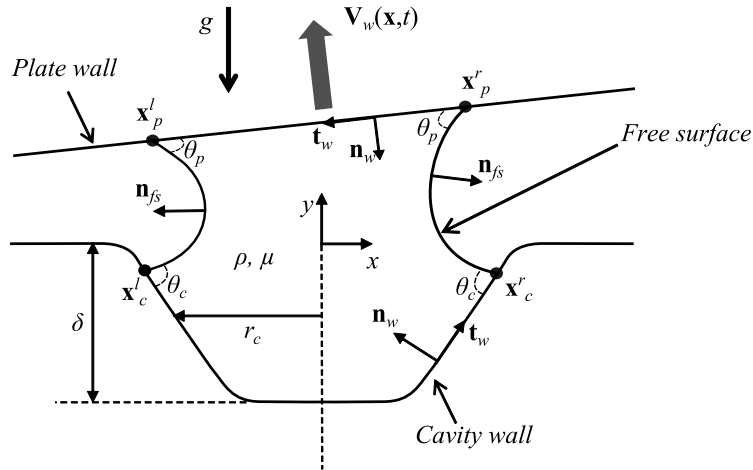


Figure 2. Sketch of the domain and geometric parameters.

The geometry in the figure represents the cross section of a groove (also called plane cavity in this work) engraved on the gravure roll. This case is the preferred option when continuous patterns (such as tracks of an electronic circuit) must be printed, because it gives better continuity and uniformity (see for example Pudas *et al.* (2004b,a); Lee *et al.* (2010b,a)).

The flow domain consists of a plane liquid bridge of a Newtonian liquid with density ρ , viscosity μ and surface tension σ , formed between the cavity and the plate. The surrounding gas phase has negligible density and viscosity (relative to the liquid properties) and a constant pressure $p_0 = 0$ which is set as reference. At $t = 0$ we consider the system in equilibrium, then the free surface is a static meniscus between the cavity and plate with static contact angles θ_c and θ_p , respectively. Quantities \mathbf{x}_c^i and \mathbf{x}_p^i represent the contact lines positions along the cavity and plate respectively, with $i = l$ denoting the left and $i = r$ the right contact lines.

Using the dimensionless variables defined in the preceding section, the Navier-Stokes equations are:

$$\begin{aligned} Re(D\mathbf{v}/Dt + \mathbf{F}_f) &= -\nabla \cdot \mathbf{T} + St\mathbf{g} \\ \nabla \cdot \mathbf{v} &= 0 \end{aligned} \quad (4)$$

In Eq. 4, $\mathbf{T} = -p\mathbf{I} + (\nabla\mathbf{v} + \nabla\mathbf{v}^T)$ is the total stress tensor (\mathbf{I} being the identity tensor), $Re = \rho\delta V_E/\mu$ is the Reynolds number and $St = \rho g\delta^2/(V_E\mu)$ the Stokes number. The term \mathbf{F}_f represents the fictitious inertial forces coming from the fact that we are using a non-inertial frame F_2 , which is translating and rotating attached to the cavity.

Along the free surfaces, we consider the liquid is free of impurities and the interface is surfactant-free, i.e. the surface tension is assumed constant. Therefore, the capillary forces that enters in the stress boundary condition for the momentum equations will have only normal component given by

$$\mathbf{n}_{fs} \cdot \mathbf{T} = \frac{\kappa}{Ca} \mathbf{n}_{fs}, \quad (5)$$

where $Ca = \mu V_E/\sigma$ is the capillary number and κ the mean curvature of the free surface given by $\kappa = -\nabla_s \cdot \mathbf{n}_{fs}$. In the above expression, $\nabla_s = (\mathbf{I} - \mathbf{nn}) \cdot \nabla$ is the surface gradient operator.

At the moving plate and cavity surfaces, because the contact lines slip along them, we must introduce some approximation or model to overcome the stress singularity at the contact lines (Huh and Scriven, 1971). As done by Dodds *et al.* (2009), Navier's slip boundary condition is used and a prescribed constant contact angle between the liquid interface and solid walls is imposed:

$$(\mathbf{n}_w \cdot \mathbf{T}) \cdot \mathbf{t}_w = 1/\beta(\mathbf{t}_w \cdot (\mathbf{v} - \mathbf{v}_{surf})); \quad \mathbf{n}_w \cdot \mathbf{n}_{fs} = \cos(\theta_i); \quad i = c, p \quad (6)$$

In Eq. 6, β is the dimensionless slip coefficient, as defined in Lamb (1975), and \mathbf{v}_{surf} is the velocity of the solid surface. When small, β is a good measure of the length along the surface where the fluid shows a significant slip. Away from the contact line, the fluid velocity quickly approaches the surface velocity (no-slip boundary condition). Both surfaces are considered impermeable:

$$\begin{aligned} \mathbf{v} \cdot \mathbf{n}_w &= 0, \text{ on cavity wall;} \\ (\mathbf{v} - \mathbf{V}_w) \cdot \mathbf{n}_w &= 0, \text{ on the moving plate.} \end{aligned} \quad (7)$$

Because the above flow equations and boundary conditions must be solved in a domain that is moving and deforming with time, the domain itself must be calculated as part of the solution. Then, the coordinates of the computational nodes

are introduced as new unknowns. We consider a computational mesh that always adjusts to the fluid domain and its boundaries (interface, moving and fixed solid surfaces). To achieve this, we consider the mesh as a fictitious elastic solid which deforms in response to boundary loads. As the mesh deforms, the interior nodes moves like particles of a compressible elastic material, while the boundary nodes move to track the boundaries of the problem. This is the so called ALE (Arbitrary Lagrangian Eulerian) mesh motion formulation (Hughes *et al.*, 1978), because while some nodes move like fluid particles (typically the boundary nodes) others move with arbitrary velocities following some physical criteria or equations to minimize mesh distortion.

Following Cairncross *et al.* (2000), we consider that the motion of the interior nodes of the domain is governed by a quasi-static momentum equation:

$$\begin{aligned}\nabla \cdot \mathbf{S} &= 0, \\ \mathbf{S} &= \lambda_s e \mathbf{I} + 2\mu_s \mathbf{E},\end{aligned}\tag{8}$$

where \mathbf{S} is the Cauchy stress tensor in the pseudo-solid which is related to the deformation field through a Hookean constitutive equation. In Eq. 8, λ_s and μ_s are the Lamé constants of the pseudo-solid, \mathbf{E} is the Eulerian strain tensor and e the volume strain. One important issue introduced by Cairncross *et al.* (2000) was the use of a finite Eulerian strain tensor

$$\mathbf{E} = \frac{1}{2} [\nabla \mathbf{d} + \nabla \mathbf{d}^T - \nabla \mathbf{d} \cdot \nabla \mathbf{d}^T] = \frac{1}{2} [\mathbf{I} - \mathbf{F}^{-T} \mathbf{F}^{-1}],\tag{9}$$

where $\mathbf{d} = \mathbf{x} - \mathbf{X}$ is the displacement field, \mathbf{x} are the current coordinates of the nodes at time t (to be calculated), \mathbf{X} are the coordinates of the fixed free-stress reference state and $\mathbf{F} = \partial \mathbf{x} / \partial \mathbf{X} = \mathbf{I} + \partial \mathbf{d} / \partial \mathbf{X}$ is the Lagrangian deformation gradient with respect to the undeformed reference state. Finally the volume strain is $e = 3(\det(|F|^{1/3}) - 1)$, which reduces to $\text{tr}(|\nabla \mathbf{d}|)$ for small displacements. As discussed in Cairncross *et al.* (2000), the use of a finite strain tensor results in important improvements on the mesh quality, especially when it experiences large deformation and rotation as in the present work. We have compared solutions using both the small displacement and finite displacement versions of the strain tensor. The use of Eq. 9 minimized mesh distortion, therefore decreasing the number of times that computationally-expensive re-meshing procedure have to be implemented.

To solve Eq. 8 two type of boundary conditions are used. The first is a *kinematic* condition that relates the velocity of the computational nodes with the velocity of fluid particles. This boundary condition is used along moving surfaces, such as the interface and the moving plate, i.e.

$$\begin{aligned}\mathbf{n}_{fs} \cdot (\mathbf{v} - \dot{\mathbf{x}}) &= 0, \text{ at free surfaces;} \\ \mathbf{n}_w \cdot (\mathbf{v} - \dot{\mathbf{x}}) &= 0, \text{ at moving plate.}\end{aligned}\tag{10}$$

In the above expressions $\dot{\mathbf{x}}$ represents the velocity of the computational nodes and \mathbf{v} the fluid velocity on that boundary. The second type of boundary conditions imposed on Eq. 8 are equations that describe the shape of given surface. For example, along the cavity wall, the nodal coordinates must satisfy (Dodds *et al.*, 2009):

$$y = f(x) = -\frac{1}{2} \left[1 - \tanh \left(\frac{|x| - r_c}{r_s} \right) \right], \text{ along the cavity wall}\tag{11}$$

In Eq. 11, r_c represents the width of the cavity, measured at $y = -\delta/2$ (in dimensional units), and is used to control the aspect ratio. In addition, r_s is a parameter that controls both the curvature of the corners and the steepness of the cavity wall. Sharp corners and steep cavity walls are obtained using small values of r_s . All quantities in Eq. 11 are made dimensionless with the cavity depth δ .

3. NUMERICAL SOLUTION

The numerical technique used to solve the system of differential equations and its boundary conditions was inspired by techniques that have been used successfully to solve others fluid flow problems involving interfacial dynamics. The main ideas were taken from the works of Ubal *et al.* (2012); Sprittles and Shikhmurzaev (2012); Cairncross *et al.* (2000), in which a detailed description of the procedure to obtain the weak formulation of the governing equations is presented. Different numerical approaches discussed in the aforementioned works were combined here to construct a robust numerical tool to solve the transient free surface flow with moving contact lines; they are commented on below.

Unstructured meshes of triangles were used to tessellated the flow domain. All boundary conditions were enforced using Lagrange's multipliers, as described in Sprittles and Shikhmurzaev (2012) and Ubal *et al.* (2012). Bi-quadratic interpolating functions were used to expand the velocity, pseudo-solid displacement and (nodal coordinates) and the Lagrange's multipliers associated with each boundary condition; bi-linear continuous basis functions were used to expand the pressure field, resulting in the well known six nodes P2P1 triangular elements.

An implicit second order time integration scheme with adaptive time step was implemented. The resulting set of non-linear equations was solved using Newton's method, with the Jacobian matrix updated at each Newton's iteration to improve the convergence. In each time step, all variables were calculated simultaneously. This is a very important aspect in viscous free-surface flows, because this type of *monolithic* schemes shows better convergence and stability properties when compared with others decoupled or semi-implicit numerical procedures (Christodoulou and Scriven, 1992; Campana *et al.*, 2007).

The model was implemented in the commercial finite element software COMSOL Multiphysics (COMSOL Multiphysics, 1998-2013). The element size in different regions of the flow domain was controlled to assume the accuracy of the solution. Special care was taken near the contact lines and regions of high surface curvature. Near the contact lines, the difference between the computed θ_c and the imposed contact angle θ ($\Delta\theta = |\theta - \theta_c|$) was used as a measure of the solution accuracy, as suggested by Sprittles and Shikhmurzaev (2012). The element size near the contact line was adjusted during the computations, such that $\Delta\theta_{max} \sim 3\%$. Besides controlling the element size near the contact line, several mesh tests were also performed to verify that the solutions presented here are mesh independent.

As the liquid bridge is highly deformed during the liquid transfer process, the elements becomes distorted during calculation, compromising the solution accuracy. To control the overall mesh quality a parameter directly related to the aspect ratio of each element is computed. Whenever this control parameter becomes below a critical value, the solution stops. At this point, the last converged solution is used to define a new geometry, which is then tessellated into a new, high-quality mesh of triangles. The last converged solution is interpolated on the new mesh and the time integration resumes. The simulations here conducted typically required between 9 and 14 re-meshing stages before achieving the breakup time. There is an inherent error in each geometry re-construction and further re-meshing stage. The total volume of liquid bridge was used as a control variable to verify the error associated with the re-meshing and interpolation steps. The maximum total variation of the volume between the initial and breakup times was always below to 0.1% (in most cases, it was around 0.01%). The linear system on each Newton's iteration was solved using direct solvers like PARDISO (Schenk and Gärtner, 2004), which ensured converged solutions in 3 or 4 Newton's iterations when using an appropriate initial guess.

4. RESULTS

4.1 Validation and selection of a base case

To validate our model and numerical method we first solve a similar model to just described, but for an axisymmetric trapezoidal cavity. When the moving plate was moved with a constant vertical velocity, our results reproduced those presented by Dodds *et al.* (2009). We compared interfacial shapes, contact line positions and the liquid fraction ϕ effectively transferred to the plate, finding an excellent agreement with values reported by Dodds *et al.* (2009). These results are not included here for brevity.

Before presenting a parametric study, a base case (BC) must be selected. The base case parameters were chosen considering typical values of operating conditions, geometric parameters and liquid properties. By taking $\rho = 1000 \text{ Kg/m}^3$, $\mu = 0.01 \text{ Pa}\cdot\text{s}$, $\sigma = 0.05 \text{ N/m}$, $R = 6 \text{ in} = 0.1524 \text{ m}$, $\delta = 10 \mu\text{m}$, $V_w = 10 \text{ m/s}$, the corresponding dimensionless parameters values are $R_b = 15240$, $\omega_b = 0.0025$, $Ca = 0.05$, $Re = 0.25$, $St \sim 10^{-4}$. For simplicity we have set $Ca = 0.1$, $Re = St = 0$. While the inertial effects can have impact on the flow, as shown by Dodds *et al.* (2011), we have limited our analysis to Stokes flow and focus it on the effects of other parameters. By setting $Re = 0$, the fictitious inertial forces resulting from the use of a non-inertial frame of reference can be neglected (see Section 2.2). In the base case, the cavity geometry was the same one used in Dodds *et al.* (2009), e.g. $r_c = 0.8$ and $r_s = 0.3$. The contact angles were set at $\theta_c = \theta_p = 70^\circ$. The initial gap H_0 between the plate and the top boundary of the cavity ($x = 0$) is also a parameter and it was set to $H_0 = 0.03$ for all cases. This a reasonable value to avoid extremely thin gaps at initial times and also to avoid the contact between the ends of the plate and the top surface of the cavity when the plate is under rotation. Because we cannot follow the evolution up to the filament breakup itself, a termination criterion for the simulation must be defined. The runs were stopped when the minimum bridge thickness was less than 0.03 and this instant was taken to be the breakup time t_b .

The slip parameter β is very important in the model and its effect was explored in several tests. As summary, values of $\beta > 10^{-2}$ led usually to an unrealistic large slip region near the contact line, while $\beta = 10^{-4}$, led to a strong boundary layer near the contact lines and very small contact line velocities, which required and extremely fine mesh. Therefore, all predictions presented were obtained with $\beta = 10^{-3}$; with this value the slip region was confined to a small area close the contact line and outside it, the velocity was virtually zero (i.e. no-slip condition).

4.2 Effect of the cavity aspect ratio and roll radius

In this section we analyze the effect of the cavity width and roll size in the liquid transfer process, when the top surface velocity corresponds to the expression that describes the full roll-to-roll kinematics (see Eq. 2). Predictions are shown

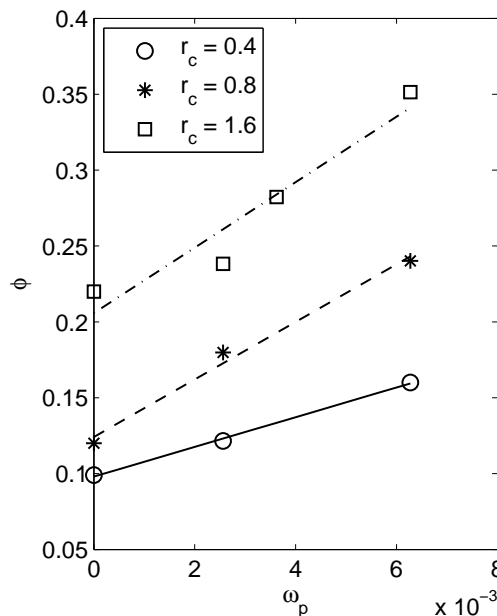


Figure 3. Liquid volume fraction transferred to the moving plate in function of the kinematic parameter ω_p and the cavity aspect ratio. Lines were obtained by linear regression.

for two values of dimensionless roll radius, e.g. $R_b = 15240$ and 2540 . Considering a cavity depth $\delta = 10 \mu\text{m}$, these values correspond to rolls radius of $R = 6$ and 1 in, respectively. The first value is a typical roll radius in gravure printing systems, while the second is representative of micro-gravure printing applications (Lee *et al.*, 2010b). As the roll radius R_b falls, the curvature of the roll begins to be comparable to the cavity size and consequently, the rotational and lateral velocities become more pronounced. To evaluate this effect, three different cases were studied: (i) pure stretching motion with $R_b = 15240$, $\omega_b = 2.5 \times 10^{-3}$ and $\omega_p = 0$ (plate velocity given by Eq. 3); (ii) complete plate kinematics (Eq. 2) with $R_b = 15240$, $\omega_p = \omega_b = 2.5 \times 10^{-3}$; and (iii) complete plate kinematic with $R_b = 2540$ and $\omega_p = \omega_b = 6.27 \times 10^{-3}$. Note that the dimensionless rotation speed changes, even though the dimensional rotation was kept constant. This is associated to the change in the roll radius, because ω_b and ω_p both scale with $1/R_b^{1/2}$. With respect to the cavity aspect ratio (or size), the values explored were $r_c = 0.4$, 0.8 and 1.6 , while r_s was kept constant, e.g. $r_s = 0.3$. The initial level of liquid at $t = 0$ was the same for all the conditions explored. This implies that the initial liquid meniscus between the plate and the cavity will be formed at different horizontal positions (x -coordinates) but at approximately the same position relative to the exterior corner. This is important to get comparable results, because the contact line mobility depends on the wall slope (curvature).

Figure 3 shows the volume fraction ϕ as a function of the parameter ω_p and for different cavity sizes r_c . The results show that wider cavities are easier to empty, because ϕ always increases with r_c ; the following discussion explain this result. The breakup of the liquid filament is controlled by two time scales. One is the time it takes the filament to thin up to the breakup limit, which is of course related with its initial thickness. The other is the time required for the contact lines to move along the cavity wall, which is related to the wettability properties (i.e. slip coefficient and contact angle) and the slope and curvature of the wall. Since the contact angles and the wall slope were constant in these simulations, the breakup is only controlled by the initial thickness. Thus, a wider initial filament thickness (wider cavity) allows the contact lines to move inside the cavity a longer distance before the breakup occurs and thus more liquid can be removed from it. Figure 4 depicts the free surfaces at breakup for all cases presented in Fig. 3.

The results also show that for a given geometry the volume of liquid transferred to the plate rises with ω_p , which is a function of roll angular velocity and radius. Higher values of ω_p are associated to higher angular velocity and smaller roll radius. Figure 4 shows how the twist and lateral displacement of the plate when $\omega_p \neq 0$ results in a non-symmetric motion of the contact lines: while the left contact line moves outside the cavity the right contact line goes deeper into it, promoting a better emptying. For $r_c = 0.4$ and 0.8 , there is a direct relation between the positions of the contact lines and the plate at the breakup to the parameter ω_p . As ω_p rises, the configuration of the filament at the breakup shows both contact lines shifted to the left of the cavity and the plate further away from the cavity. The increased lateral displacement and rotation of the plate promotes the lateral displacement of the contact lines, which helps removing liquid from the cavity but also delays the breakup. With a wide cavity ($r_c = 1.6$) the behavior is not monotonic. The breakup at the higher value of ω_p ($\omega_p = 6.27 \times 10^{-3}$) occurred faster, consequently the plate position at the breakup is closer to the cavity.

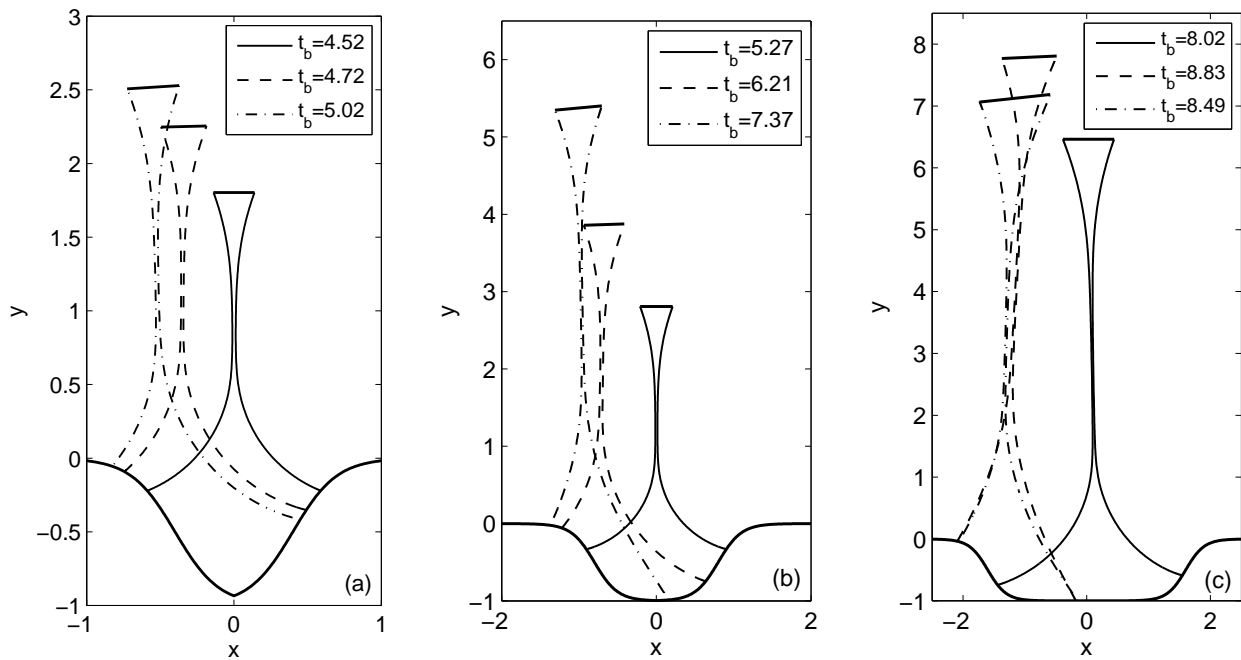


Figure 4. Free surfaces at breakup instant for the three cavity sizes: a) $r_c = 0.4$, b) $r_c = 0.8$ and c) $r_c = 1.6$. On each graph, the solid line correspond to $\omega_p = 0$, dashed line to $\omega_p = 2.5 \times 10^{-3}$ and dot dashed line to $\omega_p = 6.27 \times 10^{-3}$.

4.3 Effect of Ca number

The liquid fraction ϕ is plotted in Fig. 5 as a function of capillary number and for the same parameters used to define the BC. For comparison purposes, the predictions for pure stretching ($\omega_p = 0$) and experimental results obtained by Yin and Kumar (2006) and Chuang *et al.* (2008) are also included. The predictions for pure extensional motion, i.e. $\omega_p = 0$, present a monotonic behavior showing that the liquid volume transfer ϕ rises with capillary number. This behavior is the opposite of those observed experimentally by Yin and Kumar (2006) and Chuang *et al.* (2008). By contrast, predictions obtained with the complete plate kinematics presents a strong non-linear behavior, with local maximum and minimum points. This is due to the different responses of filament stretching dynamics and contact line pinning with capillary number, that can be understood by analyzing the evolution of the interfaces up to the breakup time for different cases, as in Fig. 6. The sequence of interfacial configurations does not correspond to the same times in all cases, but they was selected appropriately on each case to better describe the evolution.

The interface evolution at $Ca = 0.01$ is presented in Fig. 6-a. Because of the plate rotation, the radius of curvature of the left meniscus is smaller than the radius of curvature of the right interface. The curvature difference sets a strong pressure gradient that drives liquid towards the left. This lateral capillary pumping action drives liquid out of the cavity before the filament becomes elongated and the capillary action, that drives liquid from the middle of the filament towards the plate and cavity, becomes strong. Most of the filament stretching motion occurs with both contact lines out of the cavity; thus, the dynamics is roughly the same as a filament stretching between flat plates, studied by Dodds *et al.* (2009). Despite the fact that the plate is under rotation relative to the cavity, the liquid fraction is $\phi = 0.5$. This is because the liquid has almost any preference to flow towards the plate or cavity. Three dimensional calculations of Dodds *et al.* (2012) of filament stretching with a rotating upper plate have shown that is necessary a high angular velocity to break the symmetry of the liquid transfer.

To the best of our knowledge, this is the first time that such behavior is captured with numerical simulations. It was only possible because the model considers the complete kinematics that fully describes the relative motion between the substrate and the cavity, which includes extension, shearing and rotation. The low capillary number associated with the plate movement allows the development of a lateral capillary pumping that is strong enough to pull liquid out of the cavity. Although, at slightly different conditions and kinematics, this lateral capillary pumping was experimentally observed by Yin and Kumar (2006). In their experiment, a curved top surface is slide horizontally over a cavity filled with liquid. The configuration of the interface when the liquid first touches the curved plate depends on the liquid level and the gap between the cavity and plate. For a zero gap situation, and a liquid level at the top of the cavity, a very thin asymmetric meniscus is formed with strong curvature difference between the left and the right side of the liquid bridge. At that conditions, they have observed a rapid liquid flow out of the cavity. In situations at which the curvature difference is not significant they did not observe such behavior. This process is similar to the one described in our numerical results, with the difference

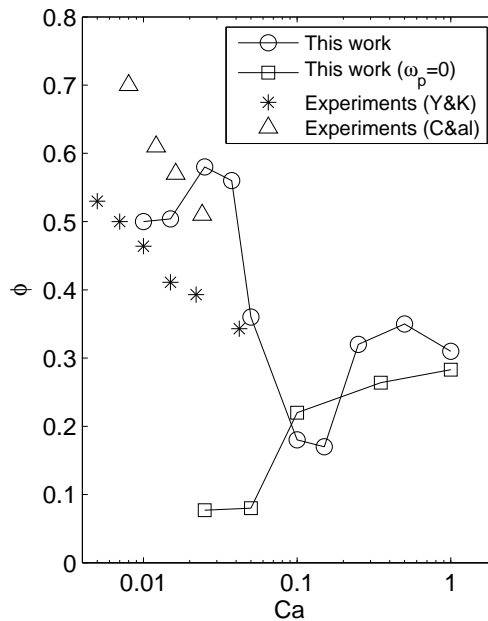


Figure 5. Mass fraction transferred to the substrate versus capillary number Ca . The other parameters correspond to the BC. Y&K: Experiments by Yin and Kumar (2006). C&al: Experiments by Chuang *et al.* (2008).

that here the curvature gradient is created by the imposed plate kinematic.

At first the liquid fraction ϕ rises with the capillary number, reaching $\phi = 0.58$ at $Ca = 0.025$. The evolution of the interface at this capillary number is shown in Fig. 6-b. The dynamic is very similar to the one just described but with one important difference. Because the capillary forces are weaker (higher Ca), the pressure gradient that drives liquid out of the cavity is smaller and this reduces the contact line velocities. As a result, when the filament begins to thin, the left contact line is outside the cavity, but the right contact line is still inside and becomes pinned at the corner of the groove during most of the filament extension. This asymmetry moves the breakup plane closer to the cavity, leading to a larger liquid volume transferred to the top plate.

From $Ca = 0.025$ to $Ca = 0.15$, the liquid fraction ϕ falls as capillary number rises. Figure 6-c shows the interface evolution at $Ca = 0.05$. The process is again similar to that at $Ca = 0.025$, but now the contact lines speeds are lower because of the weaker capillary forces. When the liquid bridge starts to thin down, the left contact line is near the corner of the groove and the right contact line is still near of the bottom surface of the cavity. The restricted movement of the left contact line causes the pinch off to occur closer to the top plate, leading to a smaller ϕ . The minimum value of ϕ occurs at $Ca = 0.15$, whose interface evolution is shown in Fig. 6-d. The capillary force is not strong enough to pump liquid out of the groove. Then, both contact lines remain inside the cavity during the entire process until breakup.

At even higher capillary number, e.g. $Ca = 0.5$ in Fig. 6-e, the contact lines at the top and bottom surfaces have very low mobility during the entire process. Thus, the wetted area on the top plate is considerably higher when compared to previous cases and, therefore, the volume of liquid attached to the top plate. As result, ϕ shows a local maximum. Finally, for $Ca = 1$ in Fig. 6-f, the contact lines are virtually frozen and its displacements is negligible during all the simulation. Although this produces an even higher wetted surface on the upper plate, less liquid is removed from the cavity and the fraction ϕ presents a small decrease.

We do not know experiments on liquid transfer from grooves available in the literature. As mentioned before, we have included data from Yin and Kumar (2006) and Chuang *et al.* (2008) to use as basis for comparison, even though their experiments do not correspond directly to the problem analyzed in this section. Yin and Kumar (2006) used a trapezoidal cavity with aspect ratio $r_c = 1.2$. They studied the liquid transfer not to a rotating cylinder, but to a curved plate that slides over the top of the cavity. They found that the liquid fraction ϕ was virtually constant at $\phi = 0.5$ for $Ca < 5 \times 10^{-3}$, and decreased monotonically for $5 \times 10^{-3} < Ca < 5 \times 10^{-2}$. Figure 5 only presents the data in the range we have explored with our model. Chuang *et al.* (2008) work with trapezoidal cells with an aspect ratio $r_c = 0.83$ and used a rotating roll over the cavity to remove the liquid from the cell, i.e. the same kinematic we have used in our analysis. However, it is important to note that they used cells in the order of millimeters and inertial and gravitational effects may become important; moreover, the parameter $Rb \sim 170$ was much smaller than the one used in our analysis. They found that ϕ falls as capillary number rises in the range explored.

Despite the differences in the imposed kinematics and geometrical parameters, the predictions show the same general trend of the experiments. It is important to note that the predicted increase of ϕ at $10^{-2} < Ca < 2 \times 10^{-2}$ is small and it would be very hard to capture experimentally. Unfortunately, we are not aware of experimental data of liquid fraction ϕ

D. M. Campana, M. S. Carvaço
Liquid transfer in gravure printing applications

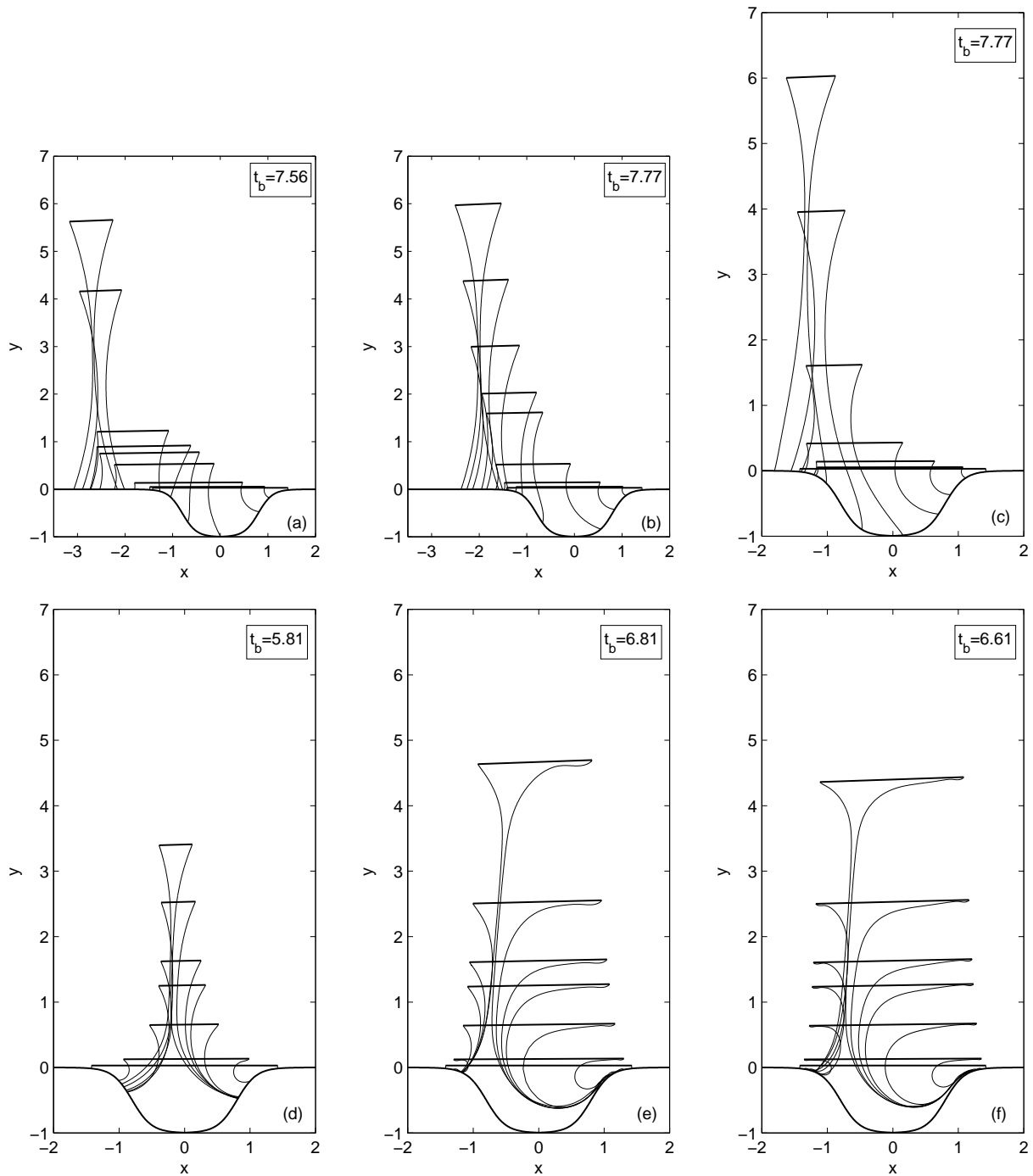


Figure 6. Free surface evolution along the emptying of the cavity for (a) $Ca = 0.01$, (b) $Ca = 0.025$, (c) $Ca = 0.05$ and (d) $Ca = 0.15$, (e) $Ca = 0.5$ and (f) $Ca = 1.0$.

at higher capillary number to validate the predicted change of behavior of ϕ as a function of Ca . Predictions obtained by considering only the extensional motion, such as those presented by Dodds *et al.* (2009) and here (with $\omega_p = 0$ in Fig. 5) has the opposite behavior, i.e. ϕ rises with capillary number. However, the rotation and lateral components of the relative motion between the substrate and cavity completely changes the dynamics of the interface deformation and, consequently, the amount of liquid transferred to the substrate.

5. Final remarks

The fundamental aspects of gravure printing can be better understood by analyzing the liquid transfer from a cell or groove to a rotating roll. In order to verify the effect of the kinematic on the dynamics of the process, we have used the complete description of motion between the substrate and a groove, which consider extension, shearing and rotation. The results show that the kinematic has a tremendous effect on the interface deformation and contact line displacements.

From an application point of view, the results considering the complete kinematics show that capillary number, i.e. liquid viscosity and substrate speed and the roll radius, have all a very strong effect on the process. When printing is performed at low capillary number, the contact lines are very mobile and a strong lateral capillary pumping action is created. This pumping is produced by the lateral and rotational motion between the surfaces, which promotes different curvatures between the right and left interfaces and a strong pressure gradient. This effect only can be observed when a complete kinematic is introduced in the model. Approximately 50% of the liquid is transferred to the substrate and, because of the lateral pumping, all liquid is removed from the cavity. The liquid not transferred to the substrate remains on the neighboring land to the cavity. As an unwanted effect, because the high contact line mobility, the printed pattern may be distorted and loss of registration may also occur. The lateral displacement of the printed pattern could be controlled by special substrate treatments to promote contact line pinning even at low capillary number, as suggested by Darhuber *et al.* (2001).

By contrast, printing at high capillary number has the advantages of a lower mobility contact lines, which lead to less distortion in the transferred image and better registration. This conclusion agrees with the experimental observation of Darhuber *et al.* (2001), which show that higher ink viscosity and extensional velocity between the surfaces avoid unwanted lateral ink redistribution during the printing. The lower transferred liquid fraction observed at high capillary number could be controlled by using smaller diameter rolls, which promotes a better liquid emptying.

Finally, the results show that use an accurate kinematic description with shearing and rotation could be only necessary at low capillary numbers, when the lateral displacement of the contact lines can be important. At high capillary number, the transferred liquid fraction is mainly controlled by the stretching and a simpler extensional motion is apparently enough to get reliable predictions. However, new experiments are needed to verify the numerical results here presented.

6. ACKNOWLEDGEMENTS

The authors would like to thank to the following institutions for financial support: *Consejo Nacional de Investigaciones Científicas y Técnicas of Argentina (CONICET)*, *Fundação de Amparo à Pesquisa do Estado do Rio de Janeiro (FAPERJ)* and the program *Industrial Partnership for Research in Interfacial and Material Engineering (IPRIME)* of the University of Minnesota.

7. REFERENCES

- Cairncross, R.A., Schunk, P.R., Baer, T.A., Rao, R.R. and Sackinger, P.A., 2000. "A finite element method for free surface flows of incompressible fluids in three dimensions. part i. boundary fitted mesh motion". *Intl J. Numer. Meth. Fluids*, Vol. 33, pp. 375–403.
- Campana, D.M., Ubal, S., Giavedoni, M.D. and Saita, F.A., 2007. "Stability of the steady motion of a liquid plug in a capillary tube". *Ind. Eng. Chem. Res.*, Vol. 46, pp. 1803–1809.
- Christodoulou, K.N., Kistler, S.F. and Schunk, P.R., 1997. *Advances in computational methods for free-surface flows*. Chapman Hall, London, UK.
- Christodoulou, K.N. and Scriven, L.E., 1992. "Discretization of free surface flows and other moving boundary problems". *J. Comp. Physics*, Vol. 99, No. 1, pp. 39–55.
- Chuang, H.K., Lee, C.C. and Liu, T.J., 2008. "An experimental study of the pick-up of scaled-up gravure cells". *Int. Polym. Process.*, Vol. 23, pp. 216–222.
- Chung, D.Y., Huang, J., Bradley, D. and Campbel, A.J., 2010. "High performance, flexible polymer light-emitting diodes (pled) with gravure contact printed hole injection and light emitting layers". *Organic Electronics*, Vol. 11, pp. 1088–1095.
- COMSOL Multiphysics, 1998-2013. "Comsol, <http://www.comsol.com/>". URL <http://www.comsol.com/>.
- Darhuber, A.A., Troian, S.M. and Wagner, S., 2001. "Physical mechanisms governing pattern fidelity in microscale offset printing". *J. App. Phys.*, Vol. 90, No. 7, pp. 3602–3609.

D. M. Campana, M. S. Carvaço
Liquid transfer in gravure printing applications

- Ding, J.M., Vornbrock, A.F., Ting, C. and Subramanian, V., 2009. "Patternable polymer bulk heterojunction photovoltaic cells on plastic by rotogravure printing". *Solar Energy Materials and Solar Cells*, Vol. 93, pp. 459–464.
- Dodds, S., 2011. *Stretching and slipping liquid bridges: Liquid transfer in industrial printing*. PhD Thesis, University of Minnesota.
- Dodds, S., Carvalho, M.S. and Kumar, S., 2009. "Stretching and slipping of liquid bridges near plates and cavities". *Phys. Fluids*, Vol. 21, No. 092103.
- Dodds, S., Carvalho, M.S. and Kumar, S., 2011. "Stretching liquid bridges with moving contact lines: The role of inertia". *Phys. Fluids*, Vol. 23, No. 092101.
- Dodds, S., Carvalho, M.S. and Kumar, S., 2012. "The dynamic of three-dimensional liquid bridges with pinned and moving contact lines". *J. Fluid Mech.*, Vol. 707, pp. 521–540.
- Hoda, N. and Kumar, S., 2008. "Boundary integral simulations of liquid emptying from a model gravure cell". *Phys. Fluids*, Vol. 20, No. 092106.
- Hughes, T.J.R., Liu, W.K. and Zimmermann, T.K., 1978. "Lagrangian-Eulerian finite element formulation for incompressible viscous flows". *Comput. Meths. Appl. Mech. Engrg.*, Vol. 15, No. 1, pp. 63–81.
- Huh, C. and Scriven, L.E., 1971. "Hydrodynamic model of steady movement of a solid/liquid/fluid contact line". *J. Colloid Interface Sci.*, Vol. 35, pp. 85–101.
- Krebs, F., 2009. "Fabrication and processing of polymer solar cells: A review of printing and coating techniques". *Solar Energy Materials and Solar Cells*, Vol. 93, pp. 394–412.
- Lamb, S.H., 1975. *Hydrodynamics (Sixth Edition)*. Cambridge University Press, London, UK.
- Lee, T.M., Lee, S.H., Noh, J.H., Kim, D.S. and Chun, S., 2010a. "The effect of shear force on ink transfer in gravure offset printing". *Journal of Micromechanics and Microengineering*, Vol. 20, No. 125026, pp. 1–8.
- Lee, T.M., Noh, J.H., Kim, C.H., Jo, J. and Kim, D.S., 2010b. "Development of a gravure offset printing system for the printing electrodes of flat panel display". *Thin Solid Film*, Vol. 518, pp. 3355–3359.
- Pudas, M., Hagberg, J. and Leppävuori, S., 2004a. "Gravure offset printing of polymer inks for conductors". *Prog. Org. Coat.*, Vol. 49, pp. 324–335.
- Pudas, M., Hagberg, J. and Leppävuori, S., 2004b. "Printing parameters and ink components affecting ultra-fine-line gravure-offset printing for electronics applications". *J. Eur. Ceram. Soc.*, Vol. 24, pp. 2943–2950.
- Santa-Nokki, H., Kallioinen, J., Kololuoma, T., Tuboltsev, V. and Korppi-Tommola, J., 2006. "Dynamic preparation of tio₂ films for fabrication of dye-sensitized solar cells". *Journal of Photochemistry and Photobiology A: Chemistry*, Vol. 182, pp. 187–191.
- Schenk, O. and Gärtner, K., 2004. "Solving unsymmetric sparse systems of linear equations with PARDISO". *Journal of Future Generation Computer Systems*, Vol. 20, No. 3, pp. 475–487.
- Sprittles, J.E. and Shikhmurzaev, Y.D., 2012. "Finite element framework for describing dynamic wetting phenomena". *Int. J. Numer. Meth. Fluids*, Vol. 68, p. 12571298.
- Ubal, S., Xu, B., Derby, B. and Grassia, P., 2012. "Continuous deposition of a liquid thread onto a moving substrate. numerical analysis and comparison with experiments". *Journal of Fluids Engineering*, Vol. 134, No. 2, p. 021301.
- Yin, X. and Kumar, S., 2006. "Flow visualization of the liquid-emptying process in scaled-up gravure grooves and cells". *Chem. Engng Sci.*, Vol. 61, pp. 1146–1156.

8. RESPONSIBILITY NOTICE

The authors are the only responsible for the printed material included in this paper.